The Changing-look Optical Wind of the Flaring X-Ray Transient Swift J1858.6-0814

T. Muñoz-Darias[1,2], M. Armas Padilla[1,2], F. Jiménez-Ibarra[1,2], G. Panizo-Espinar[1,2], J. Casares[1,2], D. Altamirano[3], D. J. K. Buisson[3], N. Castro Segura[3], V. A. Cúneo[1,2], N. Degenaar[4], F. A. Fogantini[5,6], C. Knigge[3], D. Mata Sánchez[7], M. Özbey Arabacı[3,8], J. Sánchez-Sierras[1,2], M. A. P. Torres[1,2,9], J. van den Eijnden[4], and F. M. Vincentelli[3]

[1] Instituto de Astrofísica de Canarias, E-38205 La Laguna, Tenerife, Spain; teo.munoz-darias@iac.es
[2] Departamento de Astrofísica, Universidad de La Laguna, E-38206 La Laguna, Tenerife, Spain
[3] Physics & Astronomy, University of Southampton, Southampton, Hampshire SO17 1BJ, UK
[4] Anton Pannekoek Institute for Astronomy, University of Amsterdam, Science Park 904, 1098 XH, Amsterdam, The Netherlands
[5] Facultad de Ciencias Astronómicas y Geofísicas, Universidad Nacional de La Plata, Paseo del Bosque s/n, 1900 La Plata, Argentina
[6] Instituto Argentino de Radioastronomía (CCT-La Plata, CONICET; CICPBA), C.C. No. 5, 1894 Villa Elisa, Argentina
[7] Jodrell Bank Centre for Astrophysics, Department of Physics and Astronomy, The University of Manchester, M13 9PL, UK
[8] Department of Astronomy & Astrophysics, Atatürk University, Erzurum, Turkey
[9] SRON, Netherlands Institute for Space Research, Sorbonnelaan 2, NL-3584 CA Utrecht, The Netherlands

Abstract

We present the discovery of an optical accretion disk wind in the X-ray transient Swift J1858.6-0814. Our 90-spectrum data set, taken with the 10.4 m Gran Telescopio Canarias telescope over eight different epochs and across five months, reveals the presence of conspicuous P-Cyg profiles in He I at 5876 Å and Hα. These features are detected throughout the entire campaign, albeit their intensity and main observational properties are observed to vary on timescales as short as 5 minutes. In particular, we observe significant variations in the wind velocity, between a few hundreds and ~2400 km s^{-1}. In agreement with previous reports, our observations are characterized by the presence of frequent flares, although the relation between the continuum flux variability and the presence/absence of wind features is not evident. The reported high activity of the system at radio waves indicates that the optical wind of Swift J1858.6-0814 is contemporaneous with the radio jet, as is the case for the handful of X-ray binary transients that have shown so far optical P-Cyg profiles. Finally, we compare our results with those of other sources showing optical accretion disk winds, with emphasis on V404 Cyg and V4641 Sgr, since they also display strong and variable optical wind features as well as similar flaring behavior.

Unified Astronomy Thesaurus concepts: Neutron stars (1108); X-ray binary stars (1811); Stellar winds (1636); Stellar accretion disks (1579); Stellar mass black holes (1611)

1. Introduction

In addition to a large variety of accretion-related observables, mostly seen in X-rays (McClintock & Remillard 2006; van der Klis 2006; Belloni et al. 2011), low-mass X-ray binaries (LMXBs) also show a complex outflow phenomenology. This initially included synchrotron radio emission from jets, either in the form of compact sources or discrete ejections (e.g., Mirabel & Rodriguez 1999; Fender et al. 2004), and subsequently X-ray winds of highly ionized material (e.g., Miller et al. 2006; Ponti et al. 2012; Díaz Trigo & Boirin 2016). These outflows can be the dominant source of power released and mass consumed/expelled by the system during some accretion phases (Fender & Muñoz-Darias 2016), and as such represent a fundamental part of the entire accretion process onto stellar-mass black holes (BHs) and neutron stars (NSs).

Furthermore, intense and sensitive spectroscopic campaigns carried out over the last few years have unveiled the presence of optical winds in several BH transients. P-Cyg profiles have been discovered in V404 Cyg (Muñoz-Darias et al. 2016, 2017; Mata Sánchez et al. 2018; see also Casares et al. 1991 for detections during the 1989 outburst) and MAXI J1820+070 (Muñoz-Darias et al. 2019b), while an archival search showed the presence of conspicuous wind signatures in several outbursts of V4641 Sgr (Muñoz-Darias et al. 2018; see Lindstrøm et al. 2005 and Chaty et al. 2003 for earlier reports). In addition, the classical systems GRO J1655-40 and GX 339-4 showed complex emission line profiles (Soria et al. 2000; Rahoui et al. 2014, respectively), while the intriguing optical

dips of Swift J1357.2-0933 (Corral-Santana et al. 2013) have recently been found to be related to disk outflows seen at high orbital inclination (Charles et al. 2019; Jiménez-Ibarra et al. 2019b). All the above, together with the near-infrared P-Cyg profiles witnessed in at least one luminous NS system (GX 13 +1; Bandyopadhyay et al. 1999; see also Homan et al. 2016), indicate that cold accretion disk winds (i.e., those detected at optical and infrared wavelengths) are a relatively common feature—perhaps ubiquitous—in the LMXB accretion phenomena. For the best studied case of V404 Cyg, these are found to have a severe impact on the accretion process and outburst evolution, with an associated mass outflow rate greatly exceeding the accretion rate, albeit this system might represent an extreme case (Muñoz-Darias et al. 2016; Casares et al. 2019).

Swift J1858.6-0814 was discovered by the BAT monitor on board the Neil Gehrels Swift Observatory (Gehrels et al. 2004) on 2018 October 25, and soon after cataloged as a new galactic X-ray binary transient (Krimm et al. 2018). Since the early phase of the outburst, it became a target of special interest owing to its remarkable flaring behavior at both X-rays (Ludlam et al. 2018) and optical wavelengths (Baglio et al. 2018; Paice et al. 2018; Vasilopoulos et al. 2018). This triggered the comparison with the BH transients V404 Cyg and V4641 Sgr by Ludlam et al. (2018), which was reinforced by telegrams reporting the presence of intrinsic X-ray absorption (Reynolds et al. 2018) and optical winds (Muñoz-Darias et al. 2019a). In this Letter, we present multiepoch, high-cadence

Table 1
Observing Log

Epoch	Observing Window (UT)	Grism[a] and Exposures	g-band Magnitude
1	24 Mar (05:14–05:49)	LR (7 × 280 s)	16.1
2	14 Apr (05:30–06:16)	LR (9 × 280 s)	15.4–15.7
3	30 Apr (04:32–05:22)	LR (10 × 280 s)	15.9–16.2
4	12 May (03:36–04:32)	LR (1 × 280 s) + HR (10 × 280 s)	15.7–16.4
5	9 Jun (03:52–04:48)	LR (1 × 280 s) + HR (10 × 280 s)	16.2–16.5
6	1 Jul (04:03–04:59)	LR (1 × 280 s) + HR (10 × 280 s)	16.2–16.4
7	6 Aug (00:00–01:52))	HR (21 × 280 s) + LR (1 × 280 s)	16.3
8	18 Aug (21:57–22:43)	HR (9 × 284 s)	15.7–16.4

Notes. All the data were taken in 2019.

[a] LR and HR indicate lower ($\sim$350 km s^{-1}) and higher ($\sim$160 km s^{-1}) resolution grism (R1000B and R2500R, respectively).

optical spectroscopic observations of Swift J1858.6-0814 showing that this system displays optical features indicating the presence of an accretion disk wind.

2. Observations and Data Reduction

We obtained optical spectroscopy using OSIRIS (Cepa et al. 2000) attached to the Gran Telescopio Canarias at the Observatorio del Roque de los Muchachos in La Palma, Spain. The target was observed in eight different epochs over a time lapse of five months within 2019 March–August. We obtained between 7 and 22 individual spectra per epoch with the grisms R1000B (4200–7400 Å) and R2500R (5575–7685 Å) depending on the night (see Table 1). This resulted in a total of 90 spectra with a time cadence of $\sim$five minutes and a velocity resolution of $\sim$350 or $\sim$160 km s^{-1} depending on the grism (measured from the FWHM of sky lines; i.e., assuming that resolution is dominated by the 1″0 slit and not the seeing). Weather conditions were good throughout the campaign, with seeing around $\sim$1″ and clear skies. Only epoch 1 was observed on a bright night at high airmass ($\sim$1.7) due to the very limited visibility window of the target at that time of the year. Across the entire campaign the slit was rotated to include a brighter field star placed $\sim$10″ southwest from the target. In order to carry out a relative flux calibration, spectra from this object were treated in the same way as those of Swift J1858.6-0814. Data were reduced, extracted, and wavelength calibrated using IRAF tools, while MOLLY and custom PYTHON routines were used for the analysis. From our g-band acquisition images (typically three per epoch and taken before the spectra) we derive magnitudes in the range of 15.4–16.5 across the entire campaign (calibrated against Pan-STARRS).

3. Results

We focus our analysis on the 5500–7200 Å spectral range covered by both the lower (R1000B) and higher resolution (R2500R) grisms. It includes the emission lines He I at 5876 Å (He I–5876), Hα (6563 Å), He I–6678, and He I–7065. The R1000B spectra (epochs 1–7) also include the Bowen blend (mainly N III at 4641 Å) and He II at 4686 Å. These emission lines are detected across epochs 2–7, while the limited data quality of epoch 1 only allows us to study Hα in great detail.
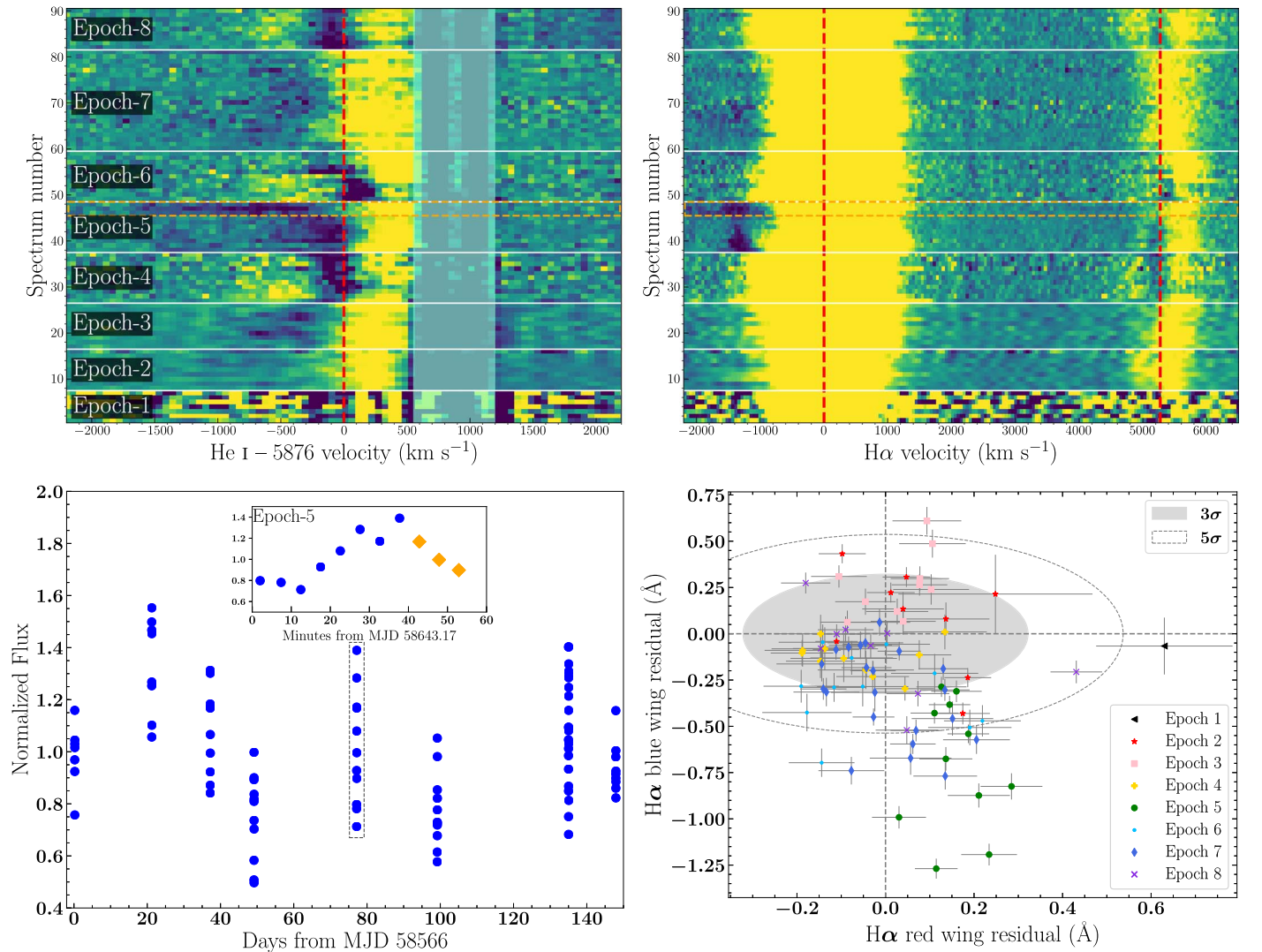
Figure 1 shows the trailed spectra (top panels) corresponding to He I–5876 (left) and Hα (plus He I–6678; right). Intensity is indicated by a color scale covering from 0.92 (deep blue) to 1.08 (bright yellow) times the continuum level. Each spectral

region was independently normalized by fitting the adjacent, local continuum with a first-order polynomial. This was done by considering relatively broad continuum regions at each side of the emission lines ($\sim\pm$10,000 km s^{-1}), masking the lines themselves and their closest continuum, as well as other contaminant features (e.g., He I–6678 for Hα). By repeating this analysis with slightly different mask configurations we estimate that the normalization process introduces an uncertainty in the continuum level of $\sim$0.3% (i.e., much lower than the $\pm$8% intensity scale used in the trailed spectra). The blue wing of the He I–5876 emission profile, typically the most sensitive to the presence of optical winds (e.g., Muñoz-Darias et al. 2016), show blueshifted absorptions in virtually every observing epoch. These absorptions (represented by deep blue traces) make the blue part of the line disappear completely during a large part of the observing campaign. We interpret this as the signature of an accretion disk wind, similar to those previously witnessed in some BH transients.

A closer look at the trailed spectra reveals that the blueshifted He I–5876 absorptions are more conspicuous between epochs 3 and 8, while Hα shows them only on epoch 5 and more weakly on epoch 7 (Figure 1, top right panel). Likewise, He I–6678 behaves in a consistent way with He I–5876, albeit it is significantly less intense than the latter, and therefore any observational feature is expected to be less marked.

Figure 2 (left panel) shows the evolution of He I–5876 using epoch 2–8 nightly average spectra. We can distinguish two groups of data by looking at the evolution of the blue wing of the emission profile (i.e., negative velocities). Epochs 3, 5, and 7 (and also 2 to some extent) show standard P-Cyg profile shapes (i.e., blueshifted absorption and redshifted emission), with the most conspicuous case (epoch 5) reaching a terminal velocity[10] of 1700 km s^{-1} and an absorption depth at the core of the profile of 95% the continuum level. An usual approach to determine the terminal velocity in a systematic way is to perform Gaussian fits to the blueshifted absorption (e.g., Muñoz-Darias et al. 2016). However, in this case the shapes are clearly non-Gaussian and hence the velocity was simply determined by visual inspection. Given the high signal-to-noise ratio of our data, we estimate this to be accurate within $\sim$100 km s^{-1} (see, e.g., insets in Figure 3). The second group

---

[10] Throughout the paper, the terminal velocity of the wind is identified as that of the blue edge of the P-Cyg absorption component. However, we note that this assumption is not always straightforward and is expected to depend on, e.g., the physical properties of the ejecta.

Figure 1. Evolution of selected emission lines and the continuum flux across the entire campaign. Top panels: trailed spectra for the He I–5876 (left) and Hα (+He I–6678; right) spectral regions in velocity scale. Intensity is indicated by a color scale covering from 0.92 (deep blue) to 1.08 (bright yellow) times the continuum level, which was previously normalized. The masked region, containing the Na interstellar doublet in the red wing of He I–5876, is indicated by a green vertical stripe. Bottom left panel: evolution of the continuum flux (6000–6250 Å) throughout the campaign. Data are represented normalized to the mean value. A zoom-in of epoch 5 (dashed-lined rectangle) is overplotted as an inset, with the orange diamonds corresponding to the spectra with the more conspicuous P-Cyg detections (dashed-lined, orange rectangles in the top panels). Bottom right panel: Hα excesses diagram for every spectrum with the exception of epoch 1, for which the epoch-averaged spectrum was used. The residuals are given in equivalent width (Å). The gray-shaded and dashed-lined circles indicate the 3σ and 5σ significance contours, respectively (see Section 3.2).

of data is formed by epochs 4, 6, and 8. They show odd profiles characterized by strong and slightly blueshifted absorption troughs reaching down to 92% the continuum level in some cases (epochs 4 and 8). However, the corresponding epoch-averaged Hα lines are dominated by standard double-peaked profiles during these times (Figure 2; right panel). The combination of a wind-induced blueshifted absorption at low velocity, together with an underlying double-peaked profile (observed in Hα) offers a viable explanation for the behavior of He I–5876 during these epochs. Under this interpretation, the emission bumps at $\sim-500\,\mathrm{km\,s^{-1}}$ would be associated with a partial absorption (by the wind) of the double-peaked disk component. If this is the case, the blue peak would appear weaker than the red one even when Hα shows the opposite behavior (e.g., epoch 4). This dimming of the blue emission suggests that even though the blue edge of the absorption indicates wind velocities of just a few hundred kilometers per second, a higher velocity component is likely present.

It is important to remark that while the Hα profile seems to be unaffected during these low-velocity wind phases, it is clearly asymmetric or even shows blueshifted absorptions during the remaining epochs. As can be seen in the trailed spectra (Figure 1), the most clear Hα wind detection also occurs on epoch 5. The wind signature is particularly strong in the last three individual spectra of this window (indicated by a dashed-lined, orange rectangle in the trailed spectra), whose averaged spectrum is shown in Figure 3. Profound P-Cyg profiles are detected in He I–5876, and especially Hα with a blueshifted absorption reaching 90% the continuum level and a blue edge velocity of $\sim2400\,\mathrm{km\,s^{-1}}$. This is larger than $\sim1700\,\mathrm{km\,s^{-1}}$ observed in He I–5876 (see insets in Figure 3).

3.1. Continuum Flux Variability

Given the strong variability observed in the line spectral profiles, we decided to study the evolution of the continuum

Muñoz-Darias et al.
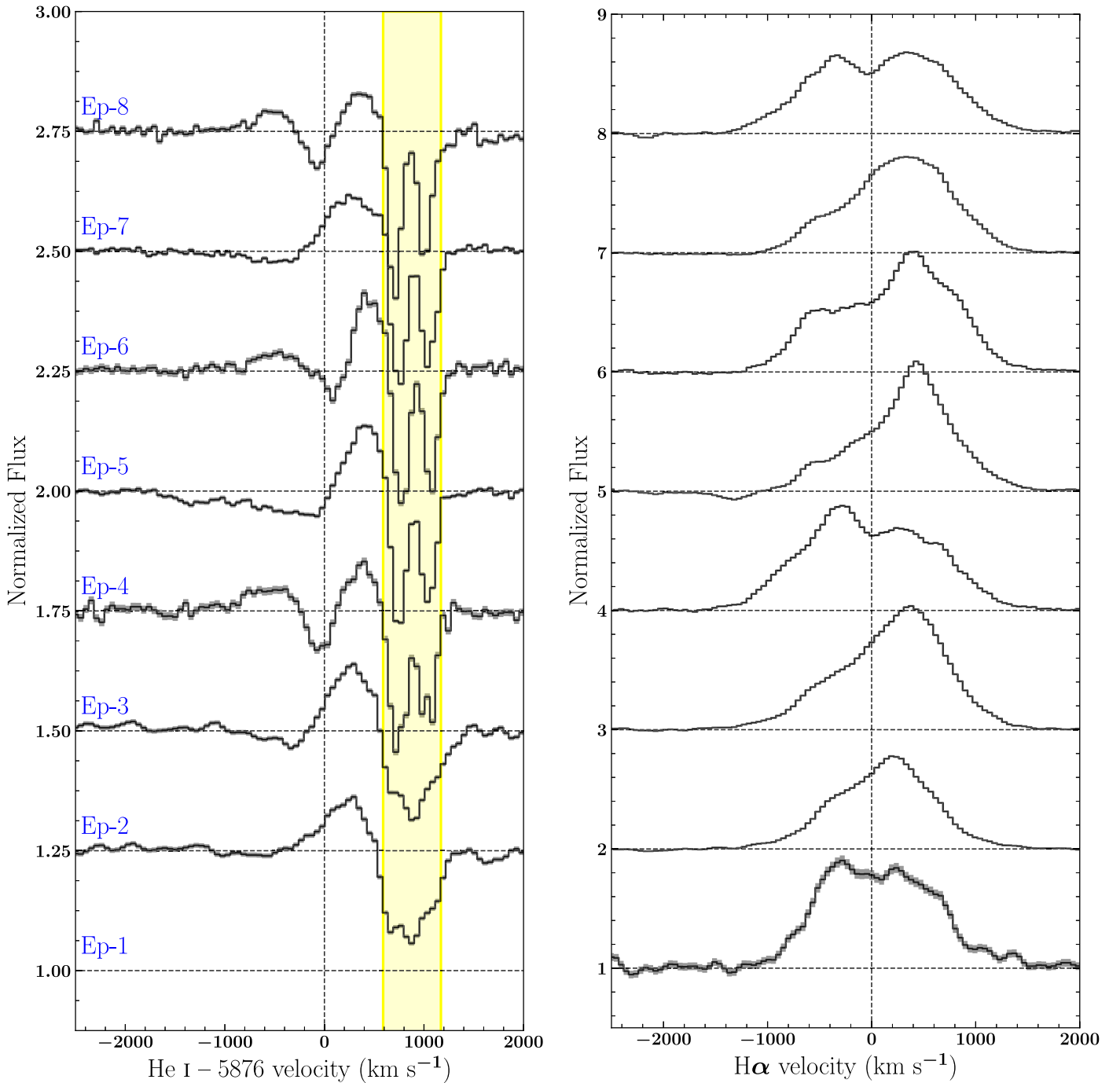
Figure 2. Evolution of the He I–5876 (left panel) and Hα (right panel) emission line profiles using epoch-averaged, normalized spectra. Data are represented using offsets of 0.25 and 1, respectively. The epoch 1 spectrum of He I–5876 is not represented due to its poor quality. The yellow shaded region indicates the spectral region contaminated by the Na doublet (interstellar).

flux. This was done by dividing each target spectrum by that of the field star included in the slit and subsequently integrating the flux from 6000 to 6250 Å. The bottom left panel of Figure 1 presents the light curve, normalized to the mean value. During the campaign, flux is observed to vary within a factor of 3, with significant variability (factor of 2) observed within each epoch. We do not find a strong correlation between the continuum flux and the properties of the wind features found at different epochs. However, there are two facts worth mentioning. On the one

hand, epoch 2, the window with the faintest wind features (He I–5876) is the one reaching the highest fluxes. On the other hand, the evolution of epoch 5 (see inset) is affected by the presence of a flare, whose detection is followed by the aforementioned conspicuous wind detections observed in this window (orange dots in the inset). In this regard, we note that even if a similar level of variability is seen in every epoch, this is generally due to fast (nonresolved) flares superposed to a smooth trend, and not to the presence of a single flare as it is the case of epoch 5.
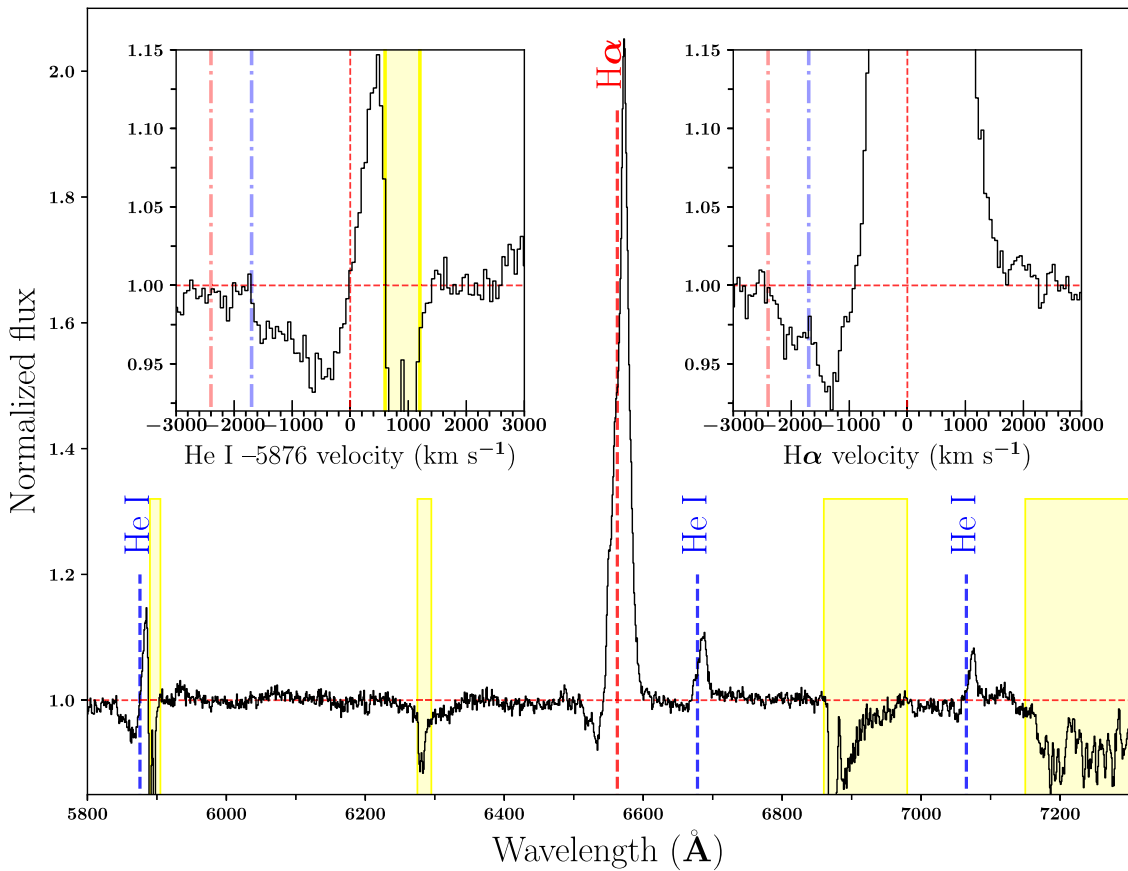
Figure 3. Average of the last three spectra obtained during epoch 5, when the deepest, high-velocity blueshifted absorption features are present. The insets show a zoom-in of He I–5876 (left) and Hα (right) in velocity scale, with the blue and red dashed–dotted lines indicating the corresponding blue edge wind velocities of 1700 km s^{-1} and 2400 km s^{-1}, respectively. The yellow shaded regions indicate spectral regions contaminated by interstellar or telluric features.

3.2. Search for Broad Emission Line Wings

Previous studies have shown that, besides P-Cyg profiles, the presence of broad emission line components can be also associated with the presence of winds. Given its strength, Hα is the best feature to search for the latter. To this end, we have computed the diagnostic diagram developed in Mata Sánchez et al. (2018) for V404 Cyg and subsequently refined in Muñoz-Darias et al. (2019b) for MAXI J1820+070, to which we refer the reader for further details. We performed a Gaussian fit to the Hα line profile masking the innermost part of the line (−500 to 500 km s^{-1} in velocity scale), subtracted the fit from the data, and measured the equivalent width (EW) of the residuals in the blue (−2000 to −1000 km s^{-1}) and red (1000 to 2000 km s^{-1}) emission line wings. Significance levels are computed by measuring the *EW of the continuum* within masks of the same width (i.e., 1000 km s^{-1}) in nearby continuum regions. They show a Gaussian distribution from which significance levels can be derived. The diagram is shown in the bottom right panel of Figure 1. In order to increase the signal-to-noise ratio, the seven spectra from epoch 1 were averaged and treated as one. As expected, the entire epoch 5 sits outside the 3σ contour, with several spectra located well beyond 5σ, within the P-Cyg region of the plot (i.e., negative blue and positive red residuals). Five spectra from epoch 7 also show significant blueshifted absorptions, as well as two from epoch 6. In addition, there are two spectra sitting on the bottom left part of the diagram, showing significant blue absorptions (>5σ). All the above can be considered wind detections based

on this method. However, none of these detections present significant red wing residuals (i.e., ≳0.55), that is, only the blueshifted part of the P-Cyg is significantly detected. As a matter of fact, the diagnostic diagram does not show any convincing detection of broad emission line wings (top right region; >5σ). Only two epoch 3 observations (out of 84) clearly exceed the 3σ level (again with nonsignificant red wing residuals), suggesting that broad emission line components are very weak or not present at all.

4. Discussion

Swift J1858.6-0814 is, after the BH systems V404 Cyg, V4641 Sgr, and MAXI J1820+070, the fourth transient LMXB showing optical P-Cyg profiles. Buisson et al. (2020) have recently reported the detection of several X-ray flares consistent with being type I X-ray bursts. If confirmed, this would make Swift J1858.6-0814 the first NS transient showing optical wind signatures, reinforcing the similarities between the outflow phenomenology seen in BH and NS transients (e.g., Ponti et al. 2014 for X-ray winds; Miller-Jones et al. 2010 for jets). In addition, the system has displayed profound, periodic dips/ eclipses implying a high inclination and strongly suggesting a relatively long orbital period of 21.8 hr (Buisson et al. 2020).

As in the previous cases, the emission line that displays the most conspicuous wind signatures is He I–5876. This is also one of the best optical wind markers in massive stars and accreting white dwarfs (e.g., Prinja & Fullerton 1994; Kafka & Honeycutt 2004). Our 90 spectra, taken over eight epochs in a

Table 2
Transient LMXBs with Optical P-Cyg Profiles

Transient	Period (hr)	Inclination (deg)	P-Cyg Depth	Terminal Velocity (km s^{-1})	Outburst	References
V404 Cyg	155.3	60–70	30%	3000	Nonstandard	1, 2
V4641 Sgr	67.6	60–70	40%	1600 (3000)[a]	Nonstandard	3, 4
Swift J1858.6-0814	21.8 (?)	Dipping/eclipsing	10%	2400	Ongoing	5, this work
MAXI J1820+070	16.9	60–81	2.5%	1800	Standard	6, 7, 8

Notes.
[a] The maximum P-Cyg terminal velocity is ∼1600 km s^{-1}. However, broad wings reaching ∼3000 km s^{-1} were also observed.
References. (1) Casares & Jonker (2014), (2) Muñoz-Darias et al. (2016), (3) Orosz et al. (2001), (4) Muñoz-Darias et al. (2018), (5) Buisson et al. (2020), (6) Torres et al. (2020), (7) Atri et al. (2020), (8) Muñoz-Darias et al. (2019b).

time lapse of five months, show that the optical wind is active during a large fraction of the time, and continuously detected in our data from (at least) epoch 2 (Figures 1 and 2). Epoch 5 is arguably the most interesting window, with strong wind signatures in both He I–5876 and Hα. The blueshifted absorptions become particularly conspicuous in the last three spectra of this epoch, showing also a significant evolution toward high velocities. The inset in the bottom left panel of Figure 1 shows the continuum flux evolution during epoch 5. It can be seen that a flare occurs in the middle of the window. Interestingly, the blueshifted Hα absorption almost disappears during the peak (top right panel in Figure 1), while the last three spectra (orange dots) correspond to the decay of the flare. This behavior strongly resembles that of V404 Cyg (e.g., Figure 2 in Muñoz-Darias et al. 2016), which showed the strongest P-Cyg profiles during a low luminosity epoch following a flare. However, the terminal velocity was not observed to vary in that case.

In V404 Cyg, the presence and variability of the P-Cyg profiles was found to be correlated with the ionization state of the outer disk, which is traced by the relative strength of He II to Hβ emission. In particular, the strongest P-Cyg profiles were found at low ionization; a conclusion that was also supported by the analysis of MAXI J1820+070 (Muñoz-Darias et al. 2019b). Here, we have also computed the flux ratio of He II to Hβ (as well as the EWs of He II and Bowen blend) in the 30 spectra taken with the lower resolution grism. Epochs 2 and 3 show variability within a factor of 2, roughly following the evolution of the continuum flux, while the single value obtained for epoch 5 is in the lower end of the sample. However, as in the case of the continuum flux variability, we do not find a clear correlation with the presence/absence of wind features. Nevertheless, given the lack of high-cadence coverage in He II and the similarities between epoch 5 and the behavior seen in V404 Cyg, we cannot rule out that ionization effects are a key factor in determining the visibility and properties of the wind.

4.1. Comparison with Other LMXBs

Table 2 displays the main wind observables as well as some fundamental system parameters of the four transient LMXB with optical P-Cyg detections. As recently discussed in Hare et al. (2020), the strong flaring activity and variable X-ray absorption of Swift J1858.6-0814 (see also Ludlam et al. 2018; Reynolds et al. 2018) resembles the behavior of V404 Cyg and V4641 Sgr (see, e.g., Gallo et al. 2014; Morningstar et al. 2014; Kimura et al. 2016; Motta et al. 2017; Muñoz-Darias et al. 2018). These two objects display nonstandard outbursts characterized by sharp rising phases followed by significant luminosity drops and the

absence of steady soft states (e.g., Casares et al. 2019 for V404 Cyg). The discovery outburst of Swift J1858.6-0814 is still ongoing and it is beyond the scope of this paper to discuss the outburst evolution. Nevertheless, the source has been active in radio during the entire optical campaign (J. van den Eijnden et al. 2020, in preparation), which is one of the standard observables associated with BH (and NS to some extent) hard and intermediate states (e.g., Fender & Muñoz-Darias 2016). This is consistent with the behavior seen in V404 Cyg, V4641 Sgr, and MAXI J1820+070.

Table 2 also reports the maximum terminal velocity and blue-absorption depth observed in the four transients with optical P-Cyg detections. These values are likely biased since (among other things) the observing campaigns (e.g., number and frequency of observations) were significantly different and the wind parameters might also change from outburst to outburst. For instance, the 1989 outburst of V404 Cyg is characterized by lower wind velocities than the 2015 event (Mata Sánchez et al. 2018). Nevertheless, the numbers suggest that, from a purely observational point of view, the wind signatures of Swift J1858.6-0814 are reminiscent but not as extreme as those found in V404 Cyg and V4641 Sgr, while they significantly exceed those of MAXI J1820+070. This last source displayed a regular outburst evolution (e.g., Shidatsu et al. 2019) and has an orbital period of ∼17 hr (Torres et al. 2019). A tempting possibility that arises from Table 2 is that larger accretion disks (i.e., ∼long orbital periods) might produce stronger winds, that carry away more mass and/or angular momentum. This could impact the observed outburst evolution, which at least for the cases of V404 Cyg and V4641 Sgr deviates from the standard patterns typically seen in LMXBs (see, e.g., Dunn et al. 2010; Muñoz-Darias et al. 2014 for global studies). Clearly, more observations are required to confirm this speculation. A key system on this matter could be GRS 1915+105—the BH–LMXB with the longest orbital period (e.g., Corral-Santana et al. 2016)—which has shown some of the best examples of X-ray winds and radio jets (e.g., Neilsen & Lee 2009). Although this very extinguished source cannot be observed at optical wavelengths, sensitive, infrared spectroscopy might be able to shed light on this topic.

Finally, it is worth discussing the role of the orbital inclination in the wind detectability, since it has been found to be a key parameter for X-ray winds, which are best seen at high inclination (Ponti et al. 2012; Díaz Trigo & Boirin 2016). Table 2 shows how optical P-Cygs have only been detected in sources with relatively high inclination (≳60°; see Higginbottom et al. 2019 for a discussion on the wind geometry and detectability as a function of the line of sight). To this list one could add the BH transient Swift J1357.2-0933. This high inclination system has not shown

Muñoz-Darias et al.

standard P-Cyg profiles, but its characteristic optical dips have recently been found to be associated with broad, blueshifted absorptions indicating the presence of an outflow (Charles et al. 2019; Jiménez-Ibarra et al. 2019a).

5. Conclusions

We have detected clear optical features indicating the presence of an accretion disk wind in the X-ray transient Swift J1858.6-0814. The observational properties of the wind are similar to those observed in V404 Cyg and V4641 Sgr. These systems also share other observables with Swift J1858.6-0814, such as the presence of frequent flares and variable X-ray absorption. As is the case for other LMXBs with optical wind detections, the outflow is contemporaneous with the radio jet. This work provides additional support for systematic and sensitive optical spectroscopic studies of active X-ray binaries in order to unveil the occurrence rate, observational properties, and impact of these cold accretion disk winds.

ORCID iDs

T. Muñoz-Darias https://orcid.org/0000-0002-3348-4035
M. Armas Padilla https://orcid.org/0000-0002-4344-7334
F. Jiménez-Ibarra https://orcid.org/0000-0002-4634-1076
G. Panizo-Espinar https://orcid.org/0000-0003-1513-1460
J. Casares https://orcid.org/0000-0001-5031-0128
V. A. Cúneo https://orcid.org/0000-0002-1813-9137
F. A. Fogantini https://orcid.org/0000-0001-5628-9120
J. Sánchez-Sierras https://orcid.org/0000-0003-2276-4231
F. M. Vincentelli https://orcid.org/0000-0002-1481-1870

References

Atri, P., Miller-Jones, J. C. A., Bahramian, A., et al. 2020, MNRAS, 493, L81
Baglio, M. C., Russell, D. M., Pirbhoy, S., et al. 2018, ATel, 12180, 1
Bandyopadhyay, R. M., Shahbaz, T., Charles, P. A., & Naylor, T. 1999, MNRAS, 306, 417
Belloni, T. M., Motta, S. E., & Muñoz-Darias, T. 2011, BASI, 39, 409
Buisson, D. J. K., Hare, J., Guver, T., et al. 2020, ATel, 13563, 1
Casares, J., Charles, P. A., Jones, D. H. P., Rutten, R. G. M., & Callanan, P. J. 1991, MNRAS, 250, 712
Casares, J., & Jonker, P. G. 2014, SSRv, 183, 223
Casares, J., Muñoz-Darias, T., Mata Sánchez, D., et al. 2019, MNRAS, 488, 1356
Cepa, J., Aguiar, M., Escalera, V. G., et al. 2000, Proc. SPIE, 4008, 623
Charles, P., Matthews, J. H., Buckley, D. A. H., et al. 2019, MNRAS, 489, L47
Chaty, S., Charles, P. A., Martí, J., et al. 2003, MNRAS, 343, 169
Corral-Santana, J. M., Casares, J., Munoz-Darias, T., et al. 2013, Sci, 339, 1048
Corral-Santana, J. M., Casares, J., Muñoz-Darias, T., et al. 2016, A&A, 587, A61
Díaz Trigo, M., & Boirin, L. 2016, AN, 337, 368
Dunn, R. J. H., Fender, R. P., Körding, E. G., Belloni, T., & Cabanac, C. 2010, MNRAS, 403, 61
Fender, R., & Muñoz-Darias, T. 2016, in Lecture Notes in Physics, Vol. 905 ed. F. Haardt et al. (Berlin: Springer), 65
Fender, R. P., Belloni, T. M., & Gallo, E. 2004, MNRAS, 355, 1105
Gallo, E., Plotkin, R. M., & Jonker, P. G. 2014, MNRAS, 438, L41
Gehrels, N., Chincarini, G., Giommi, P., et al. 2004, ApJ, 611, 1005
Hare, J., Tomsick, J. A., Buisson, D. J. K., et al. 2020, ApJ, 890, 57
Higginbottom, N., Knigge, C., Long, K. S., Matthews, J. H., & Parkinson, E. J. 2019, MNRAS, 484, 4635
Homan, J., Neilsen, J., Allen, J. L., et al. 2016, ApJL, 830, L5
Jiménez-Ibarra, F., Muñoz-Darias, T., Armas Padilla, M., et al. 2019a, MNRAS, 484, 2078
Jiménez-Ibarra, F., Muñoz-Darias, T., Casares, J., Armas Padilla, M., & Corral-Santana, J. M. 2019b, MNRAS, 489, 3420
Kafka, S., & Honeycutt, R. K. 2004, AJ, 128, 2420
Kimura, M., Isogai, K., Kato, T., et al. 2016, Natur, 529, 54
Krimm, H., Barthelmy, S., Cummings, J., et al. 2018, ATel, 12151, 1
Lindstrøm, C., Griffin, J., Kiss, L. L., et al. 2005, MNRAS, 363, 882
Ludlam, R., Miller, J., Arzoumanian, Z., et al. 2018, ATel, 12158, 1
Mata Sánchez, D., Muñoz-Darias, T., Casares, J., et al. 2018, MNRAS, 481, 2646
McClintock, J. E., & Remillard, R. A. 2006, in Black Hole Binaries, ed. W. H. G. Lewin & M. van der Klis (Cambridge: Cambridge Univ. Press), 157
Miller, J. M., Raymond, J., Fabian, A., et al. 2006, Natur, 441, 953
Miller-Jones, J. C. A., Sivakoff, G. R., Altamirano, D., et al. 2010, ApJL, 716, L109
Mirabel, I. F., & Rodriguez, L. F. 1999, ARA&A, 37, 409
Morningstar, W. R., Miller, J. M., Reynolds, M. T., & Maitra, D. 2014, ApJL, 786, L20
Motta, S. E., Kajava, J. J. E., Sánchez-Fernández, C., Giustini, M., & Kuulkers, E. 2017, MNRAS, 468, 981
Muñoz-Darias, T., Casares, J., Mata Sánchez, D., et al. 2016, Natur, 534, 75
Muñoz-Darias, T., Casares, J., Mata Sánchez, D., et al. 2017, MNRAS, 465, L124
Muñoz-Darias, T., Fender, R. P., Motta, S. E., & Belloni, T. M. 2014, MNRAS, 443, 3270
Muñoz-Darias, T., Jimenez-Ibarra, F., Armas Padilla, M., et al. 2019a, ATel, 12881, 1
Muñoz-Darias, T., Jiménez-Ibarra, F., Panizo-Espinar, G., et al. 2019b, ApJL, 879, L4
Muñoz-Darias, T., Torres, M. A. P., & Garcia, M. R. 2018, MNRAS, 479, 3987
Neilsen, J., & Lee, J. C. 2009, Natur, 458, 481
Orosz, J. A., Kuulkers, E., van der Klis, M., et al. 2001, ApJ, 555, 489
Paice, J. A., Gandhi, P., Dhillon, V. S., et al. 2018, ATel, 12197, 1
Ponti, G., Fender, R. P., Begelman, M. C., et al. 2012, MNRAS, 422, L11
Ponti, G., Muñoz-Darias, T., & Fender, R. P. 2014, MNRAS, 444, 1829
Prinja, R. K., & Fullerton, A. W. 1994, ApJ, 426, 345
Rahoui, F., Coriat, M., & Lee, J. C. 2014, MNRAS, 442, 1610
Reynolds, M., Miller, J., Ludlam, R., & Tetarenko, B. 2018, ATel, 12220, 1
Shidatsu, M., Nakahira, S., Murata, K. L., et al. 2019, ApJ, 874, 183
Soria, R., Wu, K., & Hunstead, R. W. 2000, ApJ, 539, 445
Torres, M. A. P., Casares, J., Jiménez-Ibarra, F., et al. 2019, ApJL, 882, L21
Torres, M. A. P., Casares, J., Jiménez-Ibarra, F., et al. 2020, ApJL, in press (arXiv:2003.02360)
van der Klis, M. 2006, in Compact Stellar X-Ray Sources, ed. W. Lewin & M. van der Klis (Cambridge: Cambridge Univ. Press), 39
Vasilopoulos, G., Bailyn, C., & Milburn, J. 2018, ATel, 12164, 1